Investigation on Low-temperature Annealing Process of Solution-processed TiO$_2$ Electron Transport Layer for Flexible Perovskite Solar Cell

Xing Yu [1], Xiaoping Zou [1,*], Jin Cheng [1], Dan Chen [2,3], Yujun Yao [1], Chuangchuang Chang [1], Baoyu Liu [1], Junqi Wang [1], Zixiao Zhou [1] and Guangdong Li [1]

[1]   Beijing Advanced Innovation Center for Materials Genome Engineering, Research Center for Sensor Technology, Beijing Key Laboratory for Sensor, MOE Key Laboratory for Modern Measurement and Control Technology, School of Applied Sciences, Mechanical and Electrical Engineering School, Beijing Information Science and Technology University, Beijing 100101, China; nimingyx1@163.com (X.Y.); chengjin@bistu.edu.cn (J.C.); yyj10zy@gmail.com (Y.Y.); changcc037@gmail.com (C.C.); liubaoyu0214@163.com (B.L.); 13126706081@163.com (J.W.); zzxfpp111@163.com (Z.Z.); LGD1511455720@163.com (G.L.)

[2]   State Key Laboratory on Integrated Optoelectronics, Institute of Semiconductors, Chinese Academy of Sciences, Beijing 100083, China; chendan1988@semi.ac.cn

[3]   Center of Materials Science and Optoelectronics Engineering, University of Chinese Academy of Sciences, Beijing 100049, China

*   Correspondence: xpzou2014@163.com; Tel.: +86-1364-105-6404

check for updates

Abstract: Flexible perovskite solar cells (PSCs) have received increasing attention in wearable and portable devices over the past ten years. The low-temperature process of electron transport layer plays a key role in fabricating flexible PSCs. In this paper, we improve the performance of flexible PSCs by controlling the thermodynamic procedure in the low-temperature annealing process of solution-processed TiO$_2$ layers and modulating the precursor concentration of (6,6)-phenyl c$_{61}$ butyric acid methyl ester (PC$_{61}$BM) deposited on fluorine-doped tin oxide (FTO)/TiO$_2$ substrate. The results show that slowing down evaporation rate of residual solvent and adopting PC$_{61}$BM of appropriate precursor concentration are confirmed to be effective methods to improve the performance of flexible PSCs. We also demonstrate carbon electrode-based flexible PSCs. Our work expands the feasibility of low temperature process for the development of flexible perovskite photodetectors and light-emitting diodes, as well as flexible PSCs.

Keywords: perovskite solar cells; flexible; low-temperature annealing process; solution-processed TiO$_2$ electron transport layer

1. Introduction

Organometal halide perovskite solar cells (PSCs) have aroused great interest in academia and industries [1–5]. The environmental issues concerning the footprint of PSC manufacturing processes are also of great importance [6]. Flexible PSCs expand the feasibility for the application in wearable and portable devices [7–10]. Recently, the power conversion efficiency (PCE) of flexible PSCs has rocketed to 18.4% [10].

There are many papers on low fabrication oxide. For example, Wang et al. adopted solution-processed amorphous WO$_X$ as electron selective layer for PSCs [1], and Eze et al. Fabricated efficient planar PSCs using solution-processed amorphous WO$_X$/fullerene C$_{60}$ as electron extraction layer [2]. In this paper, we use TiO$_2$ as electron transport layer (ETL). However, the traditional TiO$_2$

ETL-based PSCs require high temperature sintering (>400 °C) [11–15], which exceeds the thermal budget of flexible substrates such as FTO-coated polyethylene terephthalate (PET) (≤150 °C). Therefore, low temperature process of TiO$_2$ ETL has been intensively studied [16–20]. Yang et al. and Feleki et al. demonstrated magnetron sputtering and electron beam to prepare highly dense TiO$_2$ layer, respectively [16,17]. A solution process was also reported to fabricate compact TiO$_2$ ETL [18].

In 2019, based on solution process, Chu et al. studied the influence of treatment time of UV/O$_3$ process following the annealing process of TiO$_2$ film on a hotplate on the properties of TiO$_2$ ETL and discovered that 80 min-UV/O$_3$-treating endowed the flexible PSCs with a best PCE of 7.33% owing to UV/O$_3$-induced removal of residual organic solvent as well as enhanced hydrophilicity and conductivity of TiO$_2$ films [19]. In the same year, You et al. investigated the effect of different solvent used to re-disperse TiO$_2$ nano-sol on the quality of solution-processed TiO$_2$ ETL prior to the annealing process of TiO$_2$ film on a hotplate and demonstrated flexible PSCs of better PCE of 15.8% based on N, N-dimethylformamide (DMF) solvent, which has high zeta potential and low surface tension [20].

In this paper, we prepare the nano TiO$_2$ films with solution process and perform the annealing process on a hotplate at low temperature (≤150 °C). We control the morphology of TiO$_2$ ETL by adjusting evaporating rate of the organic solvent in the annealing process on a hotplate, which leads to the change of thermodynamic process in the growth and formation of TiO$_2$ films. Furthermore, we optimize the ETL with PC$_{61}$BM of different precursor solution to reduce the defects on the surface of TiO$_2$ layer [21]. It is worth noting that all the exploring experiments are carried out on the rigid substrates at first, and then we prepare the carbon electrode-based flexible PSCs based on the optimized preparing process.

2. Experiments

2.1. Materials

FTO (7–8 Ω/square, Hunan Yiyang Xiangchen Tech Co., Ltd., Yiyang, China), low-temperature TiO$_2$ nanoparticle (LT-TiO$_2$ NP) (Shanghai Mater Win New Materials Co., Ltd., Shanghai, China), PC$_{61}$BM (Xi'an Polyme Light Technology Corp., Xi'an, China), DMF (99.8%, Shanghai Mater Win New Materials Co., Ltd., Shanghai, China), dimethyl sulfoxide (DMSO, 99.8%, Shanghai Mater Win New Materials Co., Ltd., Shanghai, China), methyl ammoniur iodide (CH$_3$NH$_3$I, >99.5%, white powder in appearance, Shanghai Mater Win New Materials Co., Ltd., Shanghai, China), lead(II) iodide (PbI$_2$) (99.99%, yellow crystalline powder in appearance, Xi'an Polyme Light Technology Corp., Xi'an, China), 2, 2', 7, 7'-tetrakis-(N, N-dip-methoxyphenylamine)-9, 9'-spirobifluorene solution (Spiro-OMeTAD) (≥99.5%, yellow solution in appearance, Xi'an Polyme Light Technology Corp., Xi'an, China).

2.2. Device Fabrication

2.2.1. Cleaning of FTO Substrate

First, the FTO conductive glass was cleaned with deionized water (Beijing Information Science and Technology University, Beijing, China) and detergent with ultrasonic vibration cleaners (KQ-100E, Skymen Cleaning Technology Shenzhen Co., Ltd., Shenzhen, China) for 20 min. Next, FTO was cleaned with ethanol (Sinopharm Chemical Reagent Co., Ltd., Beijing, China) for 20 min. Then, FTO was cleaned with a mixed solution of isopropyl alcohol (Sinopharm Chemical Reagent Co., Ltd., Beijing, China), acetone (Sinopharm Chemical Reagent Co., Ltd., Beijing, China) and deionized water in a volume ratio of 1:1:1 for 20 min. Finally, the cleaned conductive glass was treated with UV light cleaner (BZS250GF-TC, Shenzhen Huiwo Technology Co., Ltd., Shenzhen, China) for 15 min.

2.2.2. Formation of Electron Transport Layer

LT-TiO$_2$ NP solution was deposited on the FTO substrate by spin-coating at 2000 rpm for 30 s and then dried at 150 °C for 20 min on a hot plate to form a nano TiO$_2$ layer.

(1) Giving the heating mode, we determine three kinds of annealing procedures (Process 1): (a) The annealing temperature was directly raised to 150 °C (Direct method); (b) The annealing temperature was raised from room temperature to 150 °C at rate of 8 °C/min (Proportional method); (c) The as-grown nano TiO_2 layer had been delayed for one hour before the annealing temperature was raised from room temperature to 150 °C at rate of 8 °C/min (Delayed method);

(2) Based on Process 1(c), we demonstrated an interface modifying procedure (Process 2): Depositing $PC_{61}BM$ of different precursor concentration (5, 10, 15, 20, 25 mg/mL) on nano TiO_2 layer by spin-coating at 1500 rpm for 30 s. After the deposition, $PC_{61}BM$ was left in the ambient condition for forty minutes to evaporate slowly with no annealing process. It is worth noting that the $PC_{61}BM$ was dissolved in chlorobenzene (Shanghai Mater Win New Materials Co., Ltd., Shanghai, China).

2.2.3. Formation of Perovskite Light-absorption Layer

First, the PbI_2 was fully dissolved in a mixed solvent of DMF and DMSO in the volume ratio of 0.95:0.05 by vigorous stirring to form 600 mg/mL precursor solution. The methyl ammonium was fully dissolved in anhydrous isopropanol to form 70 mg/mL precursor solution. Then, the PbI_2 precursor solution was deposited on the $PC_{61}BM$ layer by spin-coating at 1500 rpm for 30 s. Immediately, the CH_3NH_3I precursor solution was drop-cast on the as-grown PbI_2 film at 1500 rpm for 30 s and then dried at 150 °C for 20 min.

2.2.4. Formation of Hole Transport Layer

The hole transport layer was formed by spin-coating Spiro-OMeTAD on perovskite layer at 3000 rpm for 30 s. After the spin-coating, Spiro-OMeTAD was left in the ambient condition for 40 min to evaporate slowly with no annealing process.

### 2.2.5. Formation of Counter Electrode

The soot from the burning candle was collected with an FTO glass substrate to form a sponge-like carbon electrode, which was then pressed against the prepared hole transport layer [22].

2.3. Characterization

Field emission transmission electron microscope (FE-TEM) (Tecnai G2 F20, FEI, Hillsboro, OR, USA), field emission scanning electron microscope (FE-SEM) (SU8020, Hitachi, Tokyo, Japan) images were obtained for structural and morphological characterization of TiO_2 films, $PC_{61}BM$ layers and perovskite films. The current-voltage (J–V) curves were obtained under standard simulated air-mass (AM) 1.5 sunlight generating from a solar simulator (Sol 3A, Oriel, Newport, RI, USA). UV-vis absorption spectra were characterized by ultroviolet visible absorption spectrometer (Avantes, Apeldoorn, The Newtherlands). Photoluminescence (PL) spectrum was measured with PL testing system (LabRAW HR800, HORIBA Jobin Yvon, Paris, France). All the characterization of devices was performed in ambient atmosphere at room temperature.

3. Results and Discussion

In this paper, we investigate the effect of low temperature process of conventional TiO_2-based ETL on the performance of PSCs. Hence, we have characterized the structure of TiO_2 nanoparticles with TEM, as demonstrated in Figure 1, showing the average size of about 5 nm.
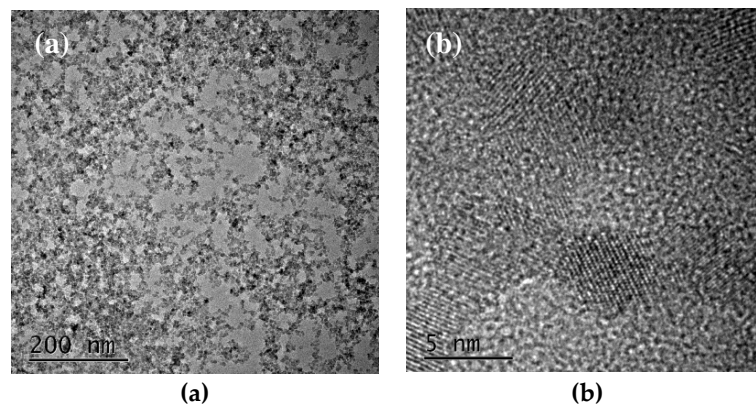
Figure 1. Transmission electron microscope (TEM) images of TiO$_2$ nanoparticles: (**a**) The low magnification; (**b**) The high magnification.

Firstly, we investigate the influence of thermodynamic process on the growth and formation of nano TiO$_2$ films. The detailed information about experiments is shown in the second paragraph of experimental Section 2.2.2. The SEM images are shown in Figure 2. The J–V curves of PSCs and the corresponding data extracted from J–V curves are shown in Figure 3 and Table 1, respectively.

It is clearly observed from Figure 2a that there are large holes remained in nano TiO$_2$ film prepared with Direct method. Figure 2b shows that these holes locate at valleys of FTO where the surface curvature changes greatly. Some voids can still be discovered from Figure 2c and d obtained from nano TiO$_2$ film prepared under Proportional method, however, they are smaller compared with Figure 2a,b. Figure 2f shows the FTO is effectively covered by nano TiO$_2$ film with few defects fabricated under Delayed method. We can also observe that the nano TiO$_2$ layer and FTO surface fit well with each other, indicating the conformal growth of nano TiO$_2$ on FTO substrate.


Figure 2. *Cont.*

(e)   (f)
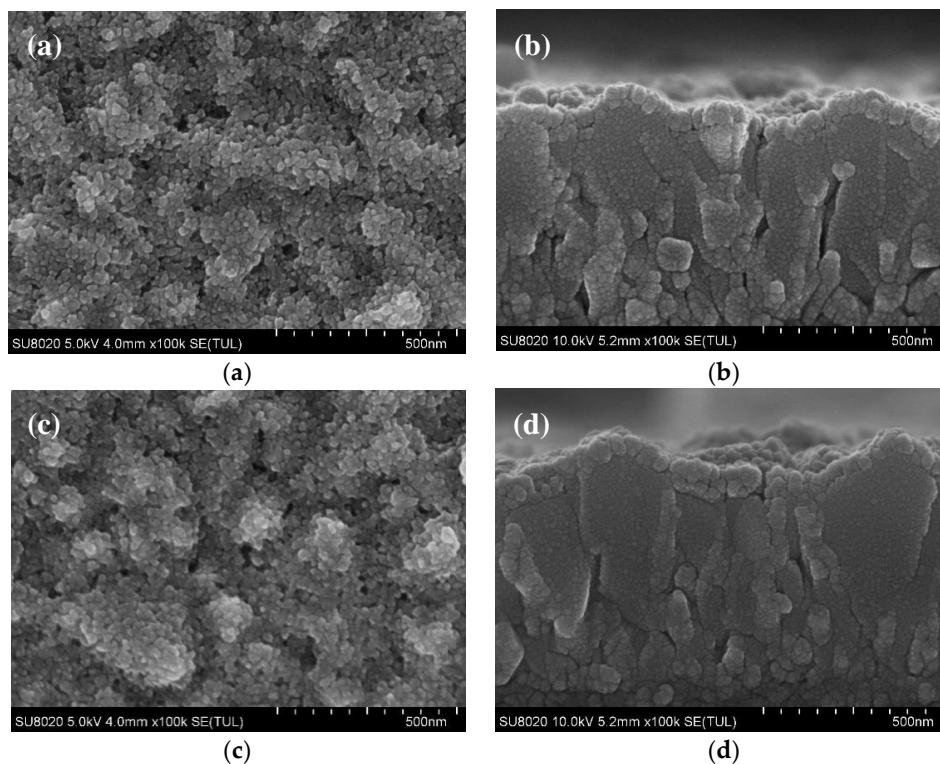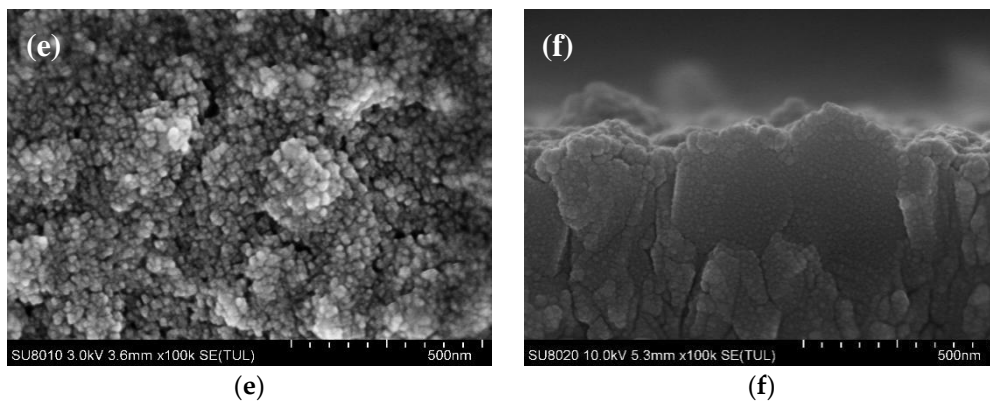
Figure 2. Scanning electron microscope (SEM) images of nano TiO$_2$ films using Process 1: (**a,c,e**) The top-view images under Direct method, Proportional method, and Delayed method, respectively; (**b,d,f**) The corresponding cross-sectional images. The meaning of Process 1, Direct method, Proportional method and Delayed method is described in the second paragraph of experimental Section 2.2.2.

We can conclude that the morphology of nano TiO$_2$ film deposited on FTO substrate can be controlled by optimizing annealing process and nano TiO$_2$ film exhibits high quality when Delayed method was introduced, which is ascribed to the slower evaporating rate of the residual solvent, resulting in conformal covering of TiO$_2$ over FTO substrate. Generally, films with fewer cracks and defects endow the PSCs with better performance, which is also confirmed by reverse scanning J–V curves of the devices in Figure 3 and data extracted from reverse scanning J–V curves in Table 1.
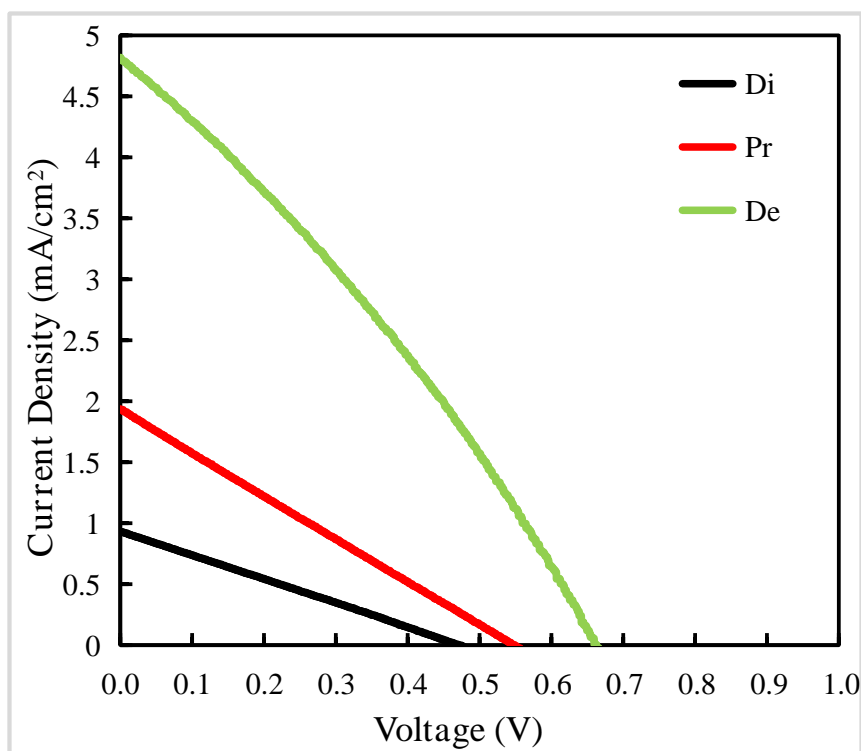
Figure 3. Reverse scanning J–V curves of PSCs based on Process 1. The letter Di, Pr, De represent films prepared with Direct method, Proportional method, and Delayed method, respectively. The device active area is 0.25 cm^2 (0.5 cm × 0.5 cm). The meaning of Process 1, Direct method, Proportional method and Delayed method is described in the second paragraph of experimental Section 2.2.2.

Table 1. Data extracted from reverse scanning J–V curves of perovskite solar cells (PSCs) based on Process 1. The letter Di, Pr, De represent films prepared with Direct method, Proportional method, and Delayed method, respectively. The device active area is 0.25 cm^2 (0.5 cm × 0.5 cm). The meaning of Process 1, Direct method, Proportional method and Delayed method is described in the second paragraph of experimental Section 2.2.2.

Samples	PCE [a] (%)	V_{oc} [b] (V)	J_{sc} [c] (mA/cm^2)	FF [d]
Di	0.26	0.55	1.94	0.27
Pr	0.11	0.47	0.93	0.25
De	0.96	0.66	4.82	0.30

Notes: a. PCE: power conversion efficiency; b. V_{OC}: open-circuit voltage; c. J_{SC}: short-circuit current; d. FF: fill factor.

Secondly, as shown in Figure 2, the TiO$_2$ nanoparticles are not connected tightly with each other, which may lead to leakage of PSCs. Therefore, we studied the effect of PC$_{61}$BM on the interface between nano TiO$_2$ layer and perovskite layer. The detailed information about experiments is shown in the third paragraph of experimental Section 2.2.2. The SEM images are shown in Figure 4.
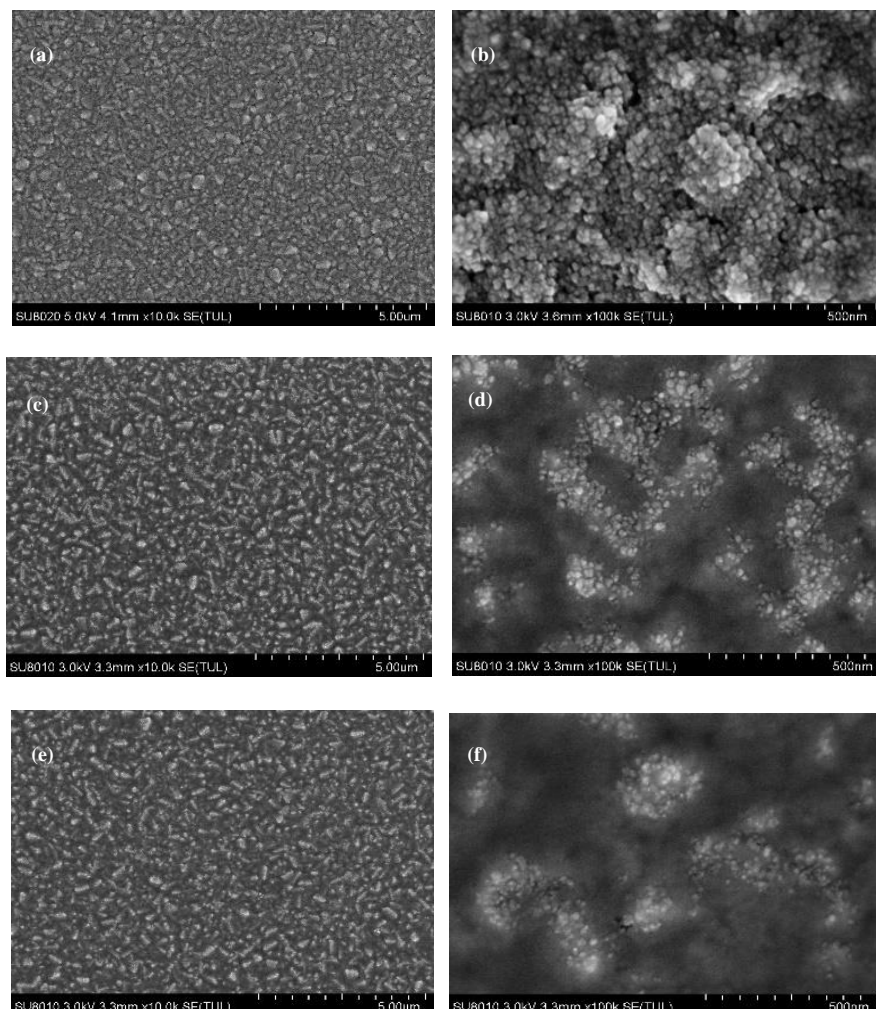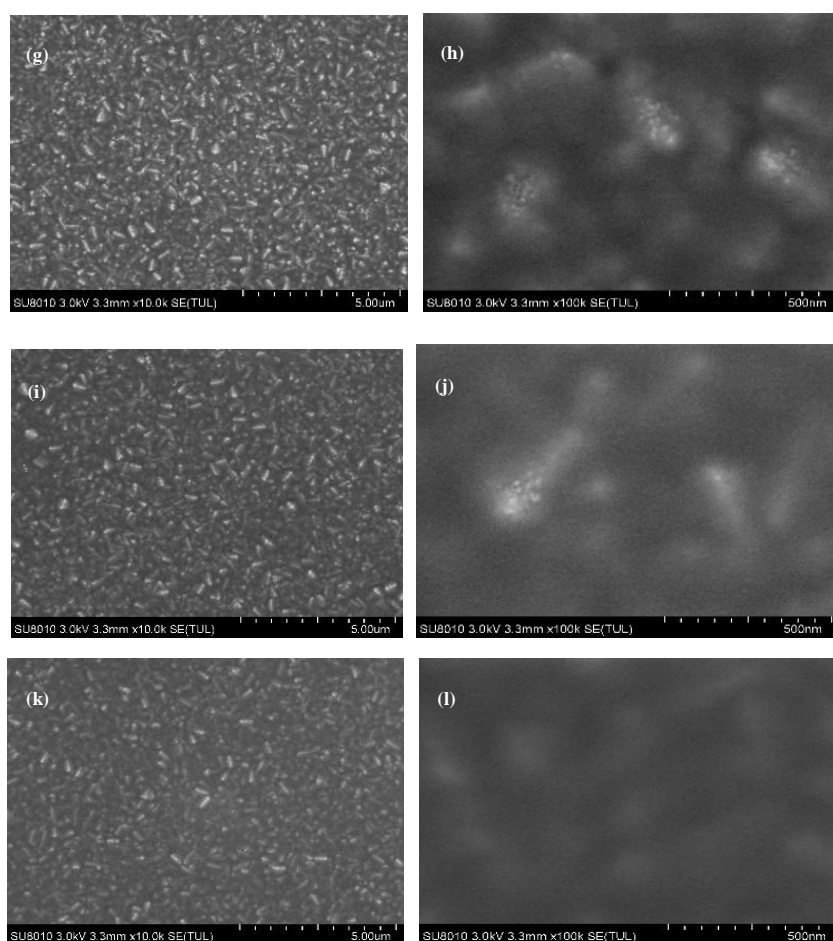

Figure 4. *Cont.*

Figure 4. SEM images of nano TiO_2 layer under Process 2: (**a**,**c**,**e**,**g**,**I**,**k**) Represent 0, 5, 10, 15, 20, 25 mg/mL, respectively, the low magnification; (**b**,**d**,**f**,**h**,**j**,**l**) The corresponding high magnification. The meaning of Process 2 is described in the third paragraph of experimental Section 2.2.2.

As shown in Figure 4d,f,h,j,l, it is clearly observed that there are some light islands distributed on the dark substrate. We can determine that the light islands are peaks of nano TiO_2 layer and the dark substrate is $PC_{61}BM$ comparing with Figure 4b. From the magnified SEM images, we can conclude that the islands disappear gradually with the concentration of $PC_{61}BM$ increasing from 5 to 25 mg/mL. When the concentration of $PC_{61}BM$ is 5 mg/mL, the $PC_{61}BM$ just filled the valleys of nano TiO_2 layers. With the concentration of $PC_{61}BM$ increased to 15 mg/mL, the nano TiO_2 film was well covered by $PC_{61}BM$ and we can hardly find the light islands, leaving few cracks. While the concentration further rises to 25 mg/mL, the nano TiO_2 layer was fully covered by $PC_{61}BM$, giving smooth and uniform film.

As demonstrated in previous report [23], it is too hard for thick ETL to transfer the electron from the absorption layer to FTO substrate and instead relatively thin ETL leads to a serious recombination of electrons and holes. Hence, we can infer that the device optimized with $PC_{61}BM$ of 15 mg/mL exhibits the best performance, in which $PC_{61}BM$ filled the most valleys of nano TiO_2 layer, leaving few cracks, preventing the contact between FTO substrate and perovskite layer and improving the electron transporting efficiency.

Finally, to investigate the influence of $PC_{61}BM$ substrate on the formation and properties of perovskite films, we studied the SEM images and absorbance spectra of perovskite films deposited on $PC_{61}BM$ of different concentration (5, 10, 15, 20, 25 mg/mL), absorbance spectra of $PC_{61}BM$ of different concentration and PL spectra of perovskite films deposited on $PC_{61}BM$ of different concentration, as shown in Figures 5–7, respectively.
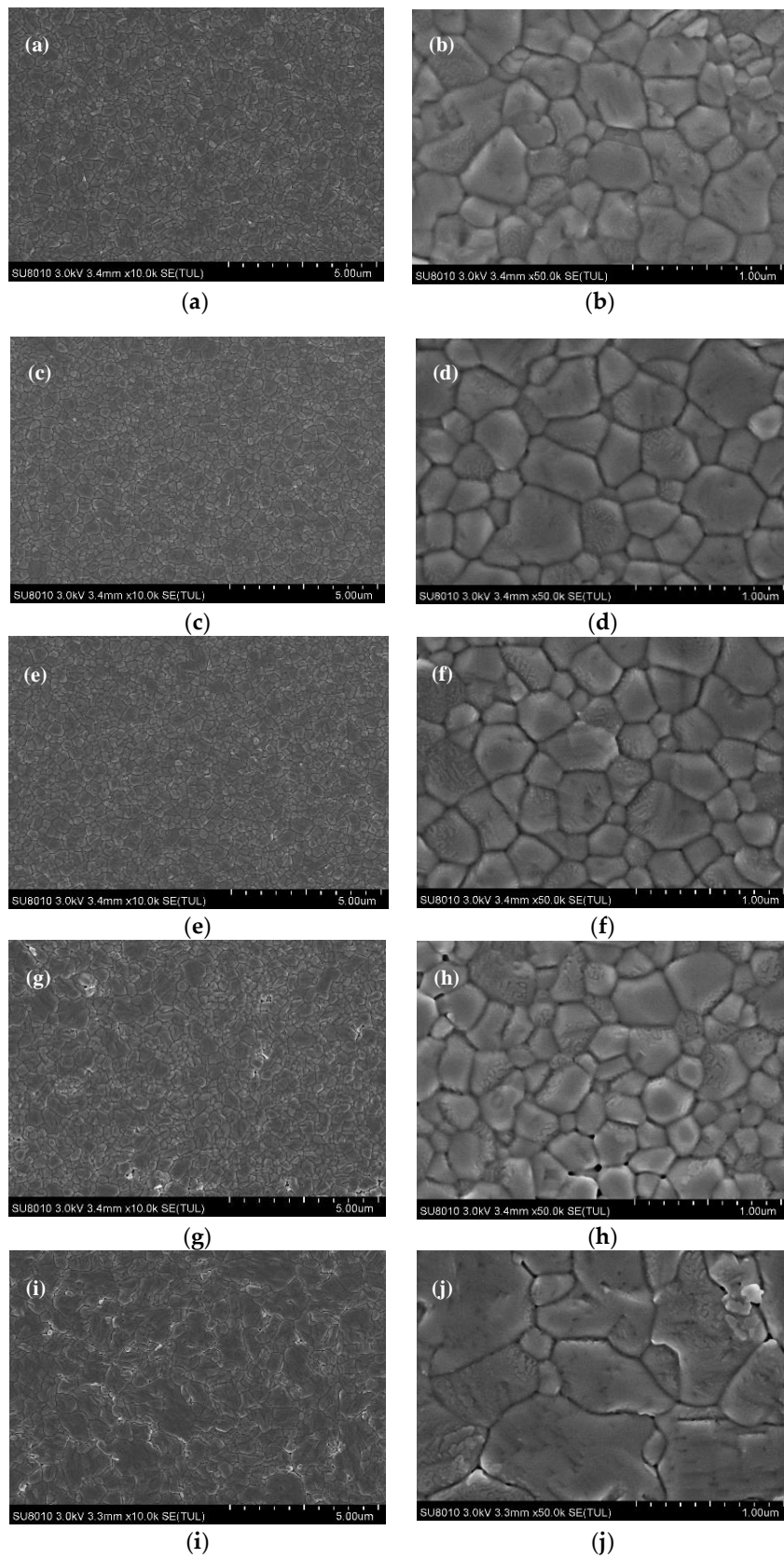
Figure 5. SEM images of perovskite film prepared on nano TiO$_2$ optimized with (6,6)-phenyl c$_{61}$ butyric acid methyl ester (PC$_{61}$BM) of different concentration: (**a**,**c**,**e**,**g**,**i**) The low magnification; (**b**,**d**,**f**,**h**,**j**) The high magnification.
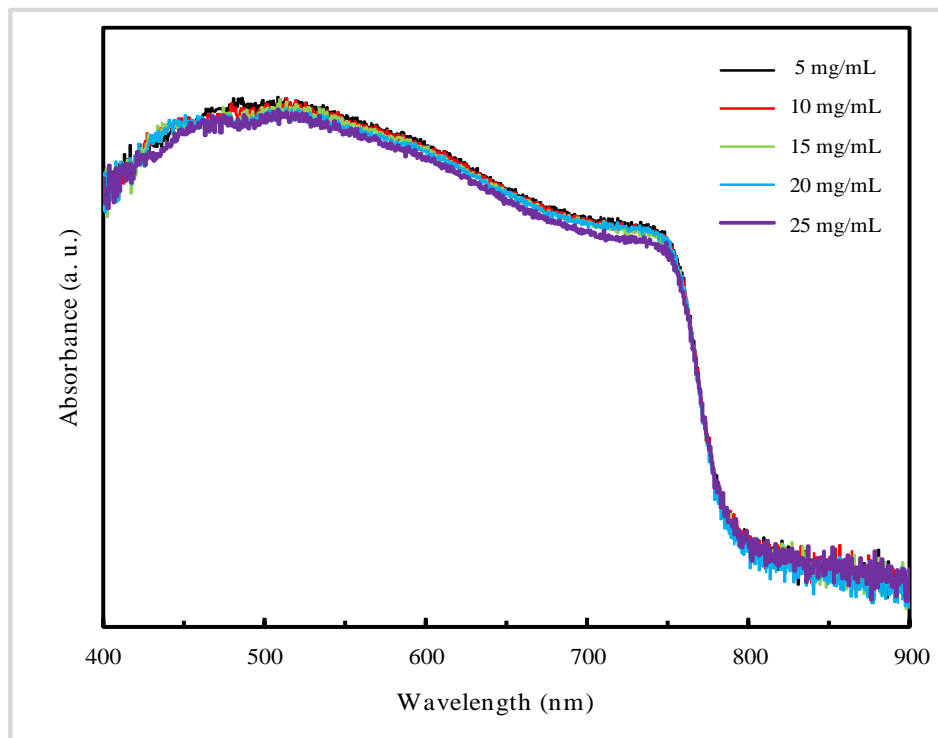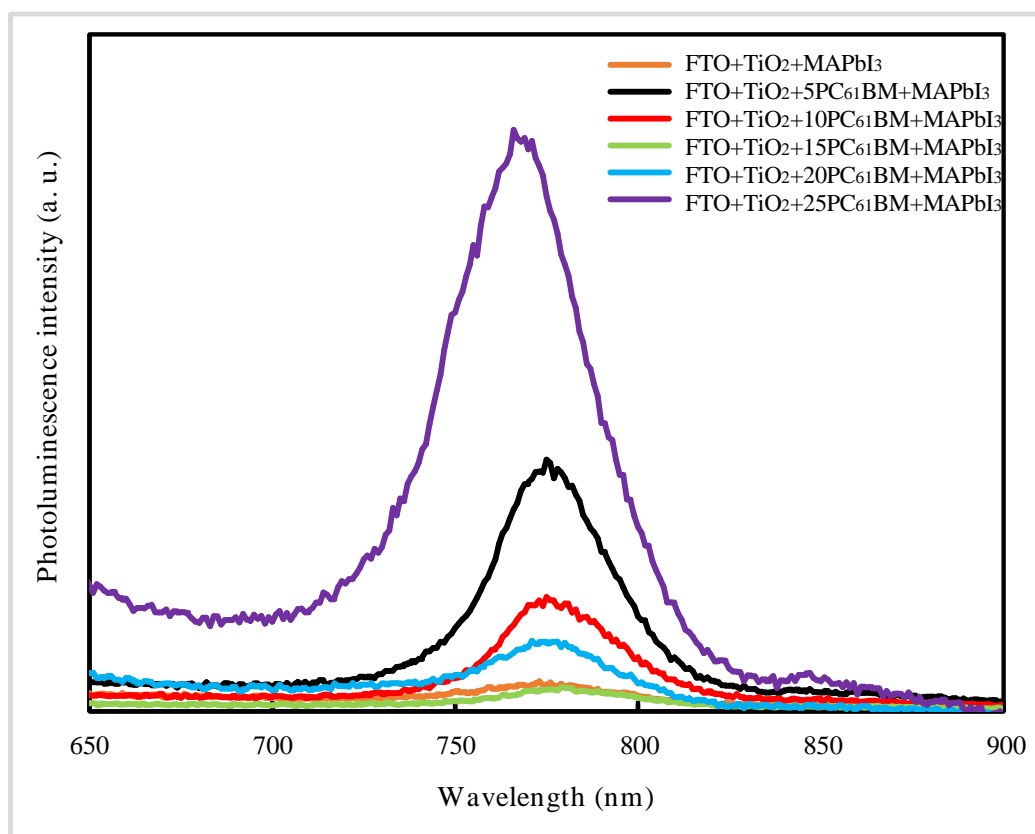
(**a**)
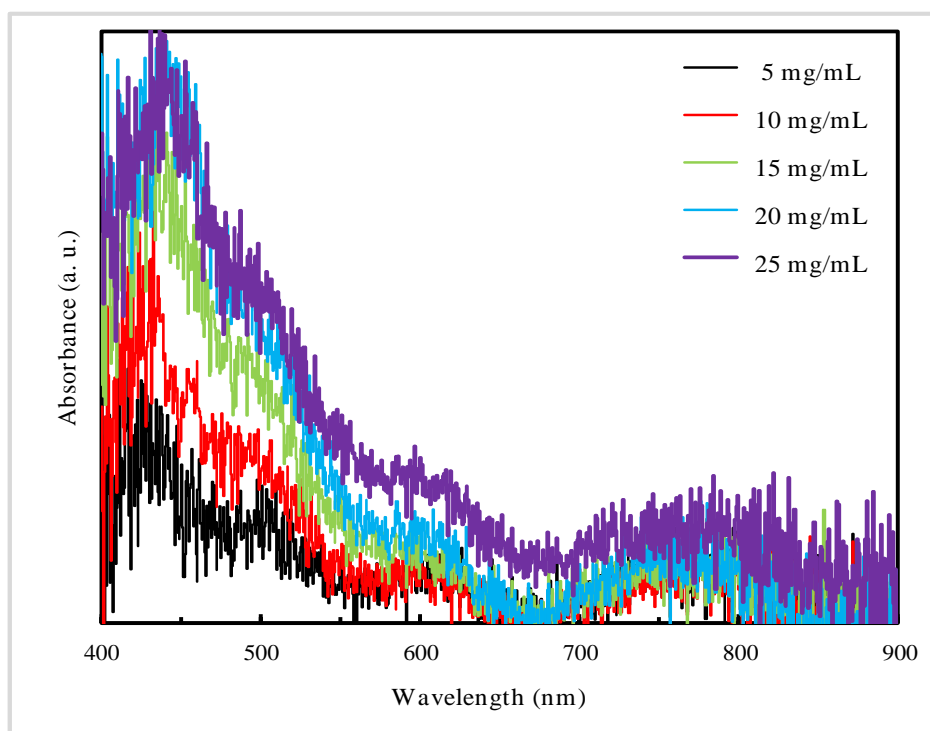
(**b**)

Figure 6. UV–vis absorption spectra of films: (**a**) Perovskite films deposited on PC$_{61}$BM layers of different concentration.; (**b**) PC$_{61}$BM films of different concentration.

Figure 7. Photoluminescence spectra of perovskite films deposited on $PC_{61}BM$ of different concentration. The number 5, 10, 15, 20, 25 represent different concentration of $PC_{61}BM$.

As shown in Figure 5, when the $PC_{61}BM$ precursor solution concentration is lower than 15 mg/mL, a good grained and uniform perovskite films were obtained. In contrast, obviously different perovskite surface morphologies are observed on 20 and 25 mg/mL $PC_{61}BM$ substrate, where the crystallinity of the perovskite films is distinctly deteriorated with serious grain boundary distortion and large holes.

From Figure 6a, we can observe that the absorption spectra signify the similar light-harvesting capabilities over 400 to 900 nm regardless of the different $PC_{61}BM$ concentration adopted. All five films exhibit approximately the same absorption edge at about 790 nm with no red-shift or blue-shift, corresponding to optical bandgap of perovskite. Particularly, perovskite films deposited on 25 mg/mL $PC_{61}BM$ manifest inferior light-harvesting capabilities, which is caused by the internal defects resulted from crystal distortion, and it is consistent with Figure 5j. From Figure 6b, we can observe that the $PC_{61}BM$ exhibits higher light-harvesting capabilities with the concentration increasing. However, perovskite films deposited on 15, 20 and 25 mg/mL $PC_{61}BM$ manifest similar absorbance, which indicates that light-harvesting capabilities of perovskite films deposited on $PC_{61}BM$ layers decrease with the precursor concentration ($\geq$15 mg/mL) of $PC_{61}BM$.

Figure 7 shows PL spectra of perovskite films deposited on $PC_{61}BM$ of different concentration. It is clearly observed that the peak of photoluminescence is fairly weak when nano TiO_2 layer has not been optimized with $PC_{61}BM$, being explained by the existence of via holes in nano TiO_2 layer, which leads to leakage. Furthermore, from Figure 7, we can observe that the PL intensity decrease as the concentration of $PC_{61}BM$ increasing from 5 to 15 mg/mL. However, when the concentration of $PC_{61}BM$ is further increased to 25 mg/mL, the PL intensity raises up again and reaches the maximum value.

As demonstrated in a previous report, the PL intensity of the films is closely related to quenching of excitons resulted from the following two reasons, radiative relaxation of excited electrons back to the ground state of perovskite and electron injection from light-absorption layer into electron transport

layer [24]. Hence, we can infer that the $PC_{61}BM$ of 15 mg/mL deposited on nano TiO_2 layer guaranteed the high-quality interface between ETL and perovskite layer, resulting in more efficient injection of electrons from perovskite layer into nano TiO_2 layer, leading to low PL intensity, which is consistent with Figure 5f.

We also have performed J–V characteristics of PSCs optimized with $PC_{61}BM$, as shown in Figure 8 and Table 2. From Figure 8 and Table 2, we can discover that following the increasing of the concentration, the PCE extracted from reverse scanning J–V curves shows up a different trend about approximately 0.81%, 2.52%, 5.48%, 3.14% and 0.26% from the perovskite solar cells with $PC_{61}BM$ concentration of 5, 10, 15, 20 and 25 mg/mL respectively. It is clearly observed that the PCE reaches the maximum value when the concentration is increased up to 15 mg/mL, and then decreases with the further increasing of the concentration, which is consistent with the above discussion.
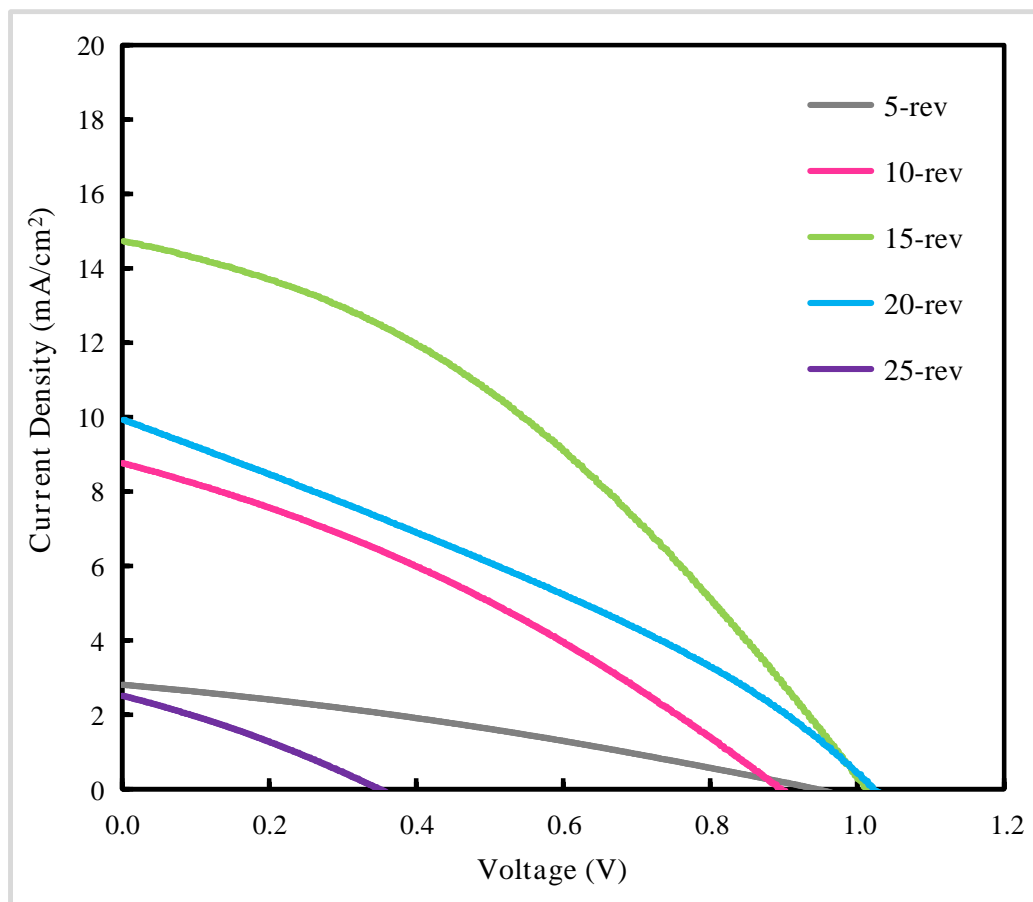
Figure 8. Reverse scanning J–V curves of perovskite solar cells optimized with different concentration of $PC_{61}BM$. -rev represents reverse scanning. The number 5, 10, 15, 20, 25 represent different concentration of $PC_{61}BM$. The device active area is 0.25 cm^2 (0.5 cm × 0.5 cm).

Table 2. Data extracted from reverse scanning J–V curves of perovskite solar cells optimized with different concentration of $PC_{61}BM$. -rev represents reverse scanning. The number 5, 10, 15, 20, 25 represent different concentration of $PC_{61}BM$. The device active area is 0.25 cm^2 (0.5 cm × 0.5 cm).

Samples	PCE [a] (%)	V_{oc} [b] (V)	J_{sc} [c] (mA/cm^2)	FF [d]
5-rev	0.81	0.94	2.81	0.31
10-rev	2.52	0.90	8.76	0.32
15-rev	5.48	1.01	14.74	0.37
20-rev	3.14	1.02	9.94	0.31
25-rev	0.26	0.35	2.52	0.29

Notes: a. PCE: power conversion efficiency; b. V_{OC}: open-circuit voltage; c. J_{SC}: short-circuit current; d. FF: fill factor.

Finally, we demonstrate the carbon electrode-based flexible solar cell of PCE of 3.24% and 2.60% for reverse and forward scanning, respectively [25]. The carbon electrode is fabricated with spongy film composed of carbon nanoparticles, which leads to unstable contact in characterization, resulting in poor device performance. The golden electrode-based device is under investigation. Moreover, we are investigating the optimization process for perovskite layer and hole transport layer and the optimization process for the interface between layers to improve the device performance.

4. Conclusions

We have discovered a method to improve the performance of PSCs by optimizing low-temperature annealing process of solution-processed TiO_2 ETL. In this work, we have received better nano TiO_2 films using Process 1c (the as-grown nano TiO_2 film had been delayed for one hour before the annealing temperature was raised from room temperature to 150 °C at rate of 8 °C/min). Moreover, the surface of nano TiO_2 film optimized with 15 mg/mL $PC_{61}BM$ endows the device with better performance. Finally, we have demonstrated the carbon electrode-based flexible perovskite solar cell, and the golden electrode-based device is under investigation. Our results can serve as a platform to fabricate high-efficiency flexible PSCs and have a potential in flexible and wearable devices.

References

1. Wang, K.; Shi, Y.; Dong, Q.; Li, Y.; Wang, S.; Yu, X.; Wu, M.; Ma, T. Low temperature and solution processed amorphous WO_x as electron selective layer for perovskite solar cells. *J. Phys. Chem. Lett.* **2015**, *6*, 755. [CrossRef]

2. Eze, V.O.; Seike, Y.; Mori, T. Efficient planar perovskite solar cells using solution-processed amorphous WO_x/fullerene C60 as electron extraction layers. *Org. Electron.* **2017**, *46*, 253–262. [CrossRef]

3. Huang, K.; Peng, Y.; Gao, Y.; Shi, J.; Li, H.; Mo, X.; Huang, H.; Gao, Y.; Ding, L.; Yang, J. High-performance flexible perovskite solar cells via precise control of electron transport layer. *Adv. Energy Mater.* **2019**, *9*, 1901419. [CrossRef]

4. Liu, C.; Zhang, L.; Zhou, X.; Gao, J.; Chen, W.; Wang, X.; Xu, B. Hydrothermally treated SnO_2 as the electron transport layer in high-efficiency flexible perovskite solar cells with a certificated efficiency of 17.3%. *Adv. Funct. Mater.* **2019**, *29*, 1807604. [CrossRef]

5. Guo, J.; Jiang, Y.; Chen, C.; Wu, X.; Kong, X.; Li, Z.; Gao, X.; Wang, Q.; Lu, X.; Zhou, G.; et al. A non-destructive transfer strategy for high-efficiency flexible perovskite solar cells. *ACS Appl. Mater. Interfaces* **2019**, *11*, 47003–47007. [CrossRef]

6. Maranghi, S.; Parisi, M.L.; Basosi, R.; Sinicropi, A. Environmental profile of the manufacturing process of perovskite photovoltaics: Harmonization of life cycle assessment studies. *Energies* **2019**, *12*, 3746. [CrossRef]

7. Li, Y.; Meng, L.; Yang, Y.M.; Xu, G.; Hong, Z.; Chen, Q.; You, J.; Li, G.; Yang, Y.; Li, Y. High-efficiency robust perovskite solar cells on ultra-thin flexible substrates. *Nat. Commun.* **2016**, *7*, 10214. [CrossRef]

8. Huang, Z.; Hu, X.; Liu, C.; Meng, X.; Huang, Z.; Yang, J.; Duan, X.; Long, J.; Zhao, Z.; Tian, L.; et al. Water-resistant and flexible perovskite solar cells via a glued interfacial layer. *Adv. Funct. Mater.* **2019**, *29*, 1902629. [CrossRef]

9. Liu, Z.; Li, S.; Wang, X.; Cui, Y.; Qin, Y.; Leng, S.; Xu, Y.; Yao, K.; Huang, H. Interfacial engineering of front-contact with finely tuned polymer interlayers for high-performance large-area flexible perovskite solar cells. *Nano Energy* **2019**, *62*, 734–744. [CrossRef]

10. Feng, J.; Zhu, X.; Yang, Z.; Zhang, X.; Niu, J.; Wang, Z.; Zou, S.; Priya, S.; Liu, S.; Yang, D. Record efficiency stable flexible perovskite solar cell using effective additive assistant strategy. *Adv. Mater.* **2018**, *30*, 1801418. [CrossRef]

11. Zhang, W.; Saliba, M.; Moore, D.T.; Pathak, S.K.; Hörantner, M.T.; Stergiopoulos, T.; Stranks, S.D.; Eperon, G.E.; Alexander-Webber, J.A.; Abate, A.; et al. Ultrasmooth organic–inorganic perovskite thin-film formation and crystallization for efficient planar heterojunction solar cells. *Nat. Commun.* **2015**, *6*, 6142. [CrossRef] [PubMed]

12. Jeon, N.J.; Noh, J.H.; Kim, Y.C.; Yang, W.S.; Ryu, S.; Seok, S.I. Solvent engineering for high-performance inorganic–organic hybrid perovskite solar cells. *Nat. Mater.* **2014**, *13*, 897–903. [CrossRef] [PubMed]

13. Jeon, N.J.; Noh, J.H.; Yang, W.S.; Kim, Y.C.; Ryu, S.; Seo, J.; Seok, S.I. Compositional engineering of perovskite materials for high-performance solar cells. *Nature* **2015**, *517*, 476. [CrossRef] [PubMed]

14. Im, J.H.; Jang, I.H.; Pellet, N.; Grätzel, M.; Park, N.G. Growth of $CH_3NH_3PbI_3$ cuboids with controlled size for high-efficiency perovskite solar cells. *Nat. Nanotechnol.* **2014**, *9*, 927–932. [CrossRef]

15. Lee, J.W.; Seol, D.J.; Cho, A.N.; Park, N.G. High-efficiency perovskite solar cells based on the black polymorph of $HC(NH_2)_2 PbI_3$. *Adv. Mater.* **2014**, *26*, 4991–4998. [CrossRef]

16. Yang, D.; Yang, R.; Zhang, J.; Yang, Z.; Liu, S.; Li, C. High efficiency flexible perovskite solar cells using superior low temperature TiO_2. *Energy Environ. Sci.* **2015**, *8*, 3208–3214. [CrossRef]

17. Qiu, W.; Paetzold, U.W.; Gehlhaar, R.; Smirnov, V.; Boyen, H.G.; Tait, J.G.; Conings, B.; Zhang, W.; Nielsen, C.B.; McCulloch, L.; et al. An electron beam evaporated TiO_2 layer for high efficiency planar perovskite solar cells on flexible polyethylene terephthalate substrates. Electron beam evaporated TiO_2 layer for high efficiency planar perovskite solar cells on polyethylene terephthalate substrates. *J. Mater. Chem.* **2015**, *3*, 22824–22829.

18. Jeong, I.; Jung, H.; Park, M.; Park, J.S.; Son, H.J.; Joo, J.; Lee, J.; Ko, M.J. A tailored TiO_2 electron selective layer for high-performance flexible perovskite solar cells via low temperature UV process. *Nano Energy* **2016**, *28*, 380–389. [CrossRef]

19. Chu, Y.; Cai, H.; Huang, L.; Xing, Z.; Du, Y.; Ni, J.; Li, J.; Zhang, J. High-efficient flexible perovskite solar cells with low temperature TiO_2 layer via UV/Ozone photo-annealing treatment. *Phys. Status Solidi A* **2019**, *216*, 1800669. [CrossRef]

20. You, M.S.; Heo, J.H.; Park, J.K.; Moon, S.H.; Park, B.J.; Im, S.H. Low temperature solution processable TiO_2 nano-sol for electron transporting layer of flexible perovskite solar cells. *Sol. Energy Mater. Sol. Cells* **2019**, *194*, 1–6. [CrossRef]

21. Shao, Y.; Xiao, Z.; Bi, C.; Yuan, Y.; Huang, J. Origin and elimination of photo-current hysteresis by fullerene passivation in $CH_3NH_3PbI_3$ planar heterojunction solar cells. *Nat. Commun.* **2014**, *5*, 5784–5791. [CrossRef] [PubMed]

22. Zhang, N.; Guo, Y.; Yin, X.; He, M.; Zou, X. Spongy carbon film deposited on a separated substrate as a counter electrode for perovskite-based solar cell. *Mater. Lett.* **2016**, *182*, 248–252. [CrossRef]

23. Ke, W.; Fang, G.; Wang, J.; Qin, P.; Tao, H.; Lei, H.; Liu, Q.; Dai, X.; Zhao, X. Perovskite solar cell with an efficient TiO_2 compact film. *Appl. Mater. Interfaces* **2014**, *6*, 15959–15965. [CrossRef] [PubMed]

24. Abdi-Jalebi, M.; Dar, M.I.; Sadhanala, A.; Senanayak, S.P.; Giordano, F.; Zakeeruddin, S.M.; Grätzel, M.; Friend, R.H. Impact of mesoporous titania-perovskite interface on the performance of hybrid organic-inorganic perovskite solar cells. *J. Phys. Chem. Lett.* **2016**, *7*, 3264–3269. [CrossRef]

25. Li, G.; Zou, X.; Cheng, J.; Chen, D.; Yao, Y.; Chang, C.; Yu, X.; Zhou, Z.; Wang, J.; Liu, B. Impact of perovskite composition on film formation quality and photophysical properties for flexible perovskite solar cells. *Molecules* **2020**, *25*, 732. [CrossRef]